


# Stabilization of 3D/2D perovskite heterostructures via inhibition of ion diffusion by cross-linked polymers for solar cells with improved performance

Received: 20 June 2022

Accepted: 16 January 2023

Published online: 09 February 2023

 Check for updates

Long Luo<sup>1,8</sup>, Haipeng Zeng<sup>1,8</sup>, Zaiwei Wang<sup>2,8</sup>, Min Li<sup>1</sup>, Shuai You<sup>1</sup>, Bin Chen<sup>2</sup>, Aidan Maxwell<sup>2</sup>, Qinyou An<sup>3</sup>, Lianmeng Cui<sup>3</sup>, Deying Luo<sup>4</sup>, Juntao Hu<sup>5</sup>, Shangzhi Li<sup>1</sup>, Xueqing Cai<sup>1</sup>, Weixi Li<sup>1</sup>, Lin Li<sup>1</sup>, Rui Guo<sup>2,1</sup>, Rong Huang<sup>6</sup>, Wenxi Liang<sup>1</sup>, Zheng-Hong Lu<sup>4,5</sup>, Liqiang Mai<sup>3,7</sup>, Yaoguang Rong<sup>1,3</sup>, Edward H. Sargent<sup>2</sup> & Xiong Li<sup>1</sup>

Two-dimensional (2D) and quasi-2D modifications of three-dimensional (3D) perovskite active layers have contributed to advances in the performance of perovskite solar cells (PSCs). However, the ionic diffusion between the surface 2D and bulk 3D perovskites leads to the degradation of the 3D/2D perovskite heterostructures and limits the long-term stability of PSCs. Here we incorporate a cross-linked polymer (CLP) on the top of a 3D perovskite layer and then deposit a 2D perovskite layer via a vapour-assisted two-step process to form a 3D/CLP/2D perovskite heterostructure. Photoluminescence spectra and thickness-profiled elemental analysis indicate that the CLP stabilizes the heterostructure by inhibiting the diffusion of cations (formamidinium, FA<sup>+</sup> and 4-fluorophenylethylammonium, 4F-PEA<sup>+</sup>) between the 2D and 3D perovskites. For devices based on carbon electrodes, we report small-area devices with an efficiency of 21.2% and mini-modules with an efficiency of 19.6%. Devices retain 90% of initial performance after 4,390 hours operation under maximum power point tracking and one-sun illumination at elevated temperatures.

Organic–inorganic hybrid perovskite solar cells (PSCs) have recently undergone a rapid rise in certified power-conversion efficiencies (PCEs) to exceed 25% for sub-1 cm<sup>2</sup> PSCs<sup>1–4</sup> and 20% for perovskite solar modules (PSMs)<sup>5–7</sup>. Many of the best PSCs employ two-dimensional (2D) or

quasi-2D modified (three-dimensional) 3D perovskite (3D/2D perovskite) heterostructures, which provide defect passivation<sup>8–10</sup> and favourable band alignment<sup>11–13</sup> and thus can improve open-circuit voltage ( $V_{oc}$ ) and fill factor (FF)<sup>14–16</sup>. These 3D/2D perovskite heterostructures are

<sup>1</sup>Michael Grätzel Center for Mesoscopic Solar Cells, Wuhan National Laboratory for Optoelectronics, Huazhong University of Science and Technology, Wuhan, China. <sup>2</sup>Department of Electrical and Computer Engineering, University of Toronto, Toronto, Ontario, Canada. <sup>3</sup>State Key Laboratory of Advanced Technologies for Materials Synthesis and Processing, Wuhan University of Technology, Wuhan, China. <sup>4</sup>Department of Materials Science and Engineering, University of Toronto, Toronto, Ontario, Canada. <sup>5</sup>Department of Physics, Center for Optoelectronics Engineering Research, Yunnan University, Kunming, China. <sup>6</sup>Vacuum Interconnected Nanotech Workstation (Nano-X), Suzhou Institute of Nano-Tech and Nano-Bionics, the Chinese Academy of Sciences, Suzhou, China. <sup>7</sup>Hubei Longzhong Laboratory, Wuhan University of Technology (Xiangyang Demonstration Zone), Xiangyang, Hubei, China. <sup>8</sup>These authors contributed equally: Long Luo, Haipeng Zeng, Zaiwei Wang. ✉ e-mail: [mlq518@whut.edu.cn](mailto:mlq518@whut.edu.cn); [ygrong2022@outlook.com](mailto:ygrong2022@outlook.com); [ted.sargent@utoronto.ca](mailto:ted.sargent@utoronto.ca); [xiongli@hust.edu.cn](mailto:xiongli@hust.edu.cn)

commonly prepared by spin coating an organic cation salt solution on top of 3D perovskites and in situ formation of thin low-dimensional perovskites (such as 2D and quasi-2D) on the surface<sup>17–20</sup>. The ion diffusion between the surface 2D and bulk 3D perovskites (for example, cations in the 3D perovskite layer move towards the 2D layer) is known to contribute to the degradation of 3D/2D perovskite heterostructures under bias, illumination and heat<sup>13,21,22</sup>. Currently, the long-term operational stability of these highly efficient PSCs is limited to <2,000 hours at room temperature, and ~500 hours at elevated temperatures ( $\geq 60$  °C) under maximum power point (MPP) tracking and continuous illumination (Supplementary Table 1).

For ion diffusion within the perovskite absorbing layer, mitigation strategies have been sought after via halide compositional tuning<sup>23–25</sup>, the incorporation of large organic cations<sup>26–29</sup> and the introduction of ionic additives<sup>30–34</sup>. For ion diffusion across interfaces and the stacked layers within PSCs, the construction of interlayers has been proven effective<sup>35–39</sup>. In particular, Bi et al. chose tri-s-triazine-based graphitic carbon nitride nanosheets to form an iodide diffusion barrier layer in p–i–n PSCs<sup>35</sup>. Wang et al. deposited a chlorinated graphene oxide layer between the perovskite and hole transporting layer (HTL) in n–i–p PSCs to prevent the iodide ions in the perovskite layer from diffusing into the HTL<sup>36</sup>. However, inhibiting ion diffusion between the 3D and 2D perovskites and stabilizing the 3D/2D perovskite heterostructures remains an ongoing challenge<sup>13,21,22</sup>.

To construct a stable 3D/2D perovskite heterostructure, we propose to introduce an interlayer between the 3D and 2D perovskite layers. The interlayer needs to effectively inhibit ion diffusion and, meanwhile, not hinder charge transport between the 3D and 2D perovskite layers. For the deposition of the interlayer and 2D perovskite layer, the technique and process need to be operated without degrading or damaging the underlying layers. Comparing small molecules versus regular polymers as the interlayer, we found that a highly cross-linked polymer (CLP) was more effective at inhibiting ion diffusion and stabilizing the 3D/2D perovskite heterostructure. We selected a polymer prepared by self-polymerization of ethylene dimethacrylate (EDMA) and polyhedral oligomeric silsesquioxane (POSS) under moderate conditions ( $\leq 100$  °C) and processed the polymer layer from a solution that does not degrade the 3D perovskite. For simplicity, CLP represents the POSS–EDMA-based polymer below. At the same time, we developed a vapour-assisted two-step deposition process to form the 2D perovskite layer on the 3D perovskite/CLP bilayer, which prevented the destruction of the underlying 3D perovskite during the deposition of the 2D perovskite. We fabricated carbon-electrode-based PSCs using the 3D/CLP/2D perovskite heterostructure with an efficiency of 21.2% (aperture area of 0.16 cm<sup>2</sup>), and demonstrate a carbon-electrode-based PSM with a certified efficiency of 18.2% (aperture area of 17.1 cm<sup>2</sup>). The cell achieved a  $T_{90}$  (the time taken for device efficiency to reduce to 90% of its initial value) of 4,390 hours under one-sun illumination and MPP tracking at 60 °C, showing superior stability compared with the PSCs based on conventional 3D/2D perovskite heterostructures at elevated temperatures.

## Selection of CLP

The molecular structures of EDMA, POSS, CLP and preparation process of the 3D/CLP/2D perovskite heterostructure are presented in Fig. 1a. For the design and selection of CLP, it should inhibit the diffusion of FA<sup>+</sup> and 4F-PEA<sup>+</sup> cations between the 3D and 2D perovskite layers and stabilize the 3D/2D perovskite heterostructure. Some organic materials including small molecules and polymers were screened based on an experiment studying the reactions of lead bromide (PbBr<sub>2</sub>)/organic films with formamidinium iodide (FAI) or 4-fluorophenylethylammonium iodide (4F-PEAI) (Fig. 1b). These organic materials include a small molecular EDMA monomer; three linear polymers of polyethylene glycol (PEG), polystyrene (PS) and polymethyl methacrylate (PMMA) (Supplementary Fig. 1) and two cross-linked polymers of EDMA (pEDMA) and the CLP. We decided to investigate pEDMA and the CLP by taking

inspiration from rechargeable batteries or fuel cells, where ion diffusion is inhibited by inserting separation materials (such as POSS- and EDMA-based polymers) as proton exchange membranes<sup>40–43</sup>. POSS consists of a rigid, cubic Si–O–Si cage-type core with eight ethylene groups that can bridge the linear EDMA chains in various directions via olefin polymerization. Approximately 3 mol% POSS dispersed in EDMA provides abundant cross-linking points and leads to the formation of a polymer film with highly cross-linked networks<sup>44–46</sup>. When the self-polymerization was carried out on a glass substrate, a uniform and free-standing transparent CLP film was obtained (Supplementary Fig. 2). The self-polymerization reaction was confirmed by Fourier transform infrared spectroscopy (FTIR) (Supplementary Fig. 3). Moreover, the CLP film was found to be insoluble in polar solvents such as H<sub>2</sub>O, isopropanol (IPA) and dimethylformamide (DMF) (Supplementary Fig. 4 and Supplementary Video 1).

Pristine PbBr<sub>2</sub> films are transparent and colourless. However, PbBr<sub>2</sub> films dipped in FAI or 4F-PEAI solutions rapidly turn brown or yellow. X-ray diffraction (XRD) measurements verified the formation of 3D FAPb(I<sub>x</sub>Br<sub>1-x</sub>)<sub>3</sub> (brown) and 2D 4F-PEA<sub>2</sub>Pb(I<sub>x</sub>Br<sub>1-x</sub>)<sub>4</sub> (yellow)<sup>47–49</sup>, as shown in Fig. 1c,d. For PbBr<sub>2</sub> films covered by PEG, PS, PMMA and EDMA monomers, similar phenomena were observed. This indicates that these small molecules and linear polymers are not ideal candidates for inhibiting the diffusion of FA<sup>+</sup> and 4F-PEA<sup>+</sup> cations. On the contrary, the PbBr<sub>2</sub>/pEDMA and PbBr<sub>2</sub>/CLP films maintained their original colour after dipping in FAI or 4F-PEAI solution. The XRD patterns show the PbBr<sub>2</sub> films were not fully transformed into 3D FAPb(I<sub>x</sub>Br<sub>1-x</sub>)<sub>3</sub> or 2D 4F-PEA<sub>2</sub>Pb(I<sub>x</sub>Br<sub>1-x</sub>)<sub>4</sub>, which indicates that the cross-linked pEDMA and CLP layer can effectively inhibit the diffusion of FA<sup>+</sup> and 4F-PEA<sup>+</sup> cations. Meanwhile, the formation of a small 2D diffraction peak in the PbBr<sub>2</sub>/pEDMA and PbBr<sub>2</sub>/CLP films indicates a small amount of FA<sup>+</sup> and 4F-PEA<sup>+</sup> can still pass through the CLP layer to form 3D or 2D perovskites (Fig. 1c,d and Supplementary Note 1). Our further studies show that the CLP layer is more effective at inhibiting ion diffusion and has better stability under thermal stress due to the incorporation of POSS (Supplementary Figs. 5 and 6 and Supplementary Note 2).

## Stabilization effect of CLP on perovskite heterostructures

To fabricate the conventional 3D/2D perovskite heterostructure, we deposit a (FAPbI<sub>3</sub>)<sub>0.95</sub>(MAPbBr<sub>3</sub>)<sub>0.05</sub> (formamidinium, FA; methylammonium, MA) 3D perovskite layer on a SnO<sub>2</sub>-coated ITO glass substrate and then post-treat the surface with a solution of 4-fluorophenylethylammonium iodide (4F-PEAI) in IPA solvent (Fig. 2a)<sup>8,17,50</sup>. XRD patterns in Fig. 2b show a characteristic diffraction peak at 5.2°, which indicates the formation of 2D 4F-PEA<sub>2</sub>PbI<sub>4</sub> ((4F-PEA)<sub>2</sub>FA<sub>n-1</sub>Pb<sub>n</sub>I<sub>3n+1</sub>,  $n = 1$ )<sup>17,49</sup>. After thermal ageing at 100 °C for 120 min, the 2D 4F-PEA<sub>2</sub>PbI<sub>4</sub> diffraction peak in the 3D/2D heterostructure disappears. Additionally, the photoluminescence (PL) spectra show that the emission peaks of 3D (FAPbI<sub>3</sub>)<sub>0.95</sub>(MAPbBr<sub>3</sub>)<sub>0.05</sub> and 2D 4F-PEA<sub>2</sub>PbI<sub>4</sub> are located at 800 nm and 511 nm respectively for the 3D/2D perovskite heterostructure (Fig. 2c). After thermal ageing, the emission peak of 4F-PEA<sub>2</sub>PbI<sub>4</sub> for the 3D/2D heterostructure also completely disappears. These results are indicative of the instability of the 3D/2D perovskite heterostructure, which is attributed to ion diffusion between the surface 2D and bulk 3D perovskites<sup>21,22</sup>.

To fabricate the 3D/CLP/2D perovskite heterostructure, we first deposited a 3D perovskite layer. The CLP layer is formed by spin coating a POSS and EDMA mixed solution in chlorobenzene and ethyl acetate mixed solvent on the above 3D perovskite and annealing at 100 °C for 10 min (Supplementary Fig. 7). These low-polarity solvents are compatible with 3D perovskites and thus do not induce degradation of the 3D perovskite. The thickness of the CLP layer is estimated to be <3 nm (Supplementary Fig. 8 and Supplementary Note 3). The 2D perovskite layer was deposited by a vapour-assisted two-step process<sup>51–53</sup>. Lead iodide (PbI<sub>2</sub>) was first evaporated on the CLP layer and

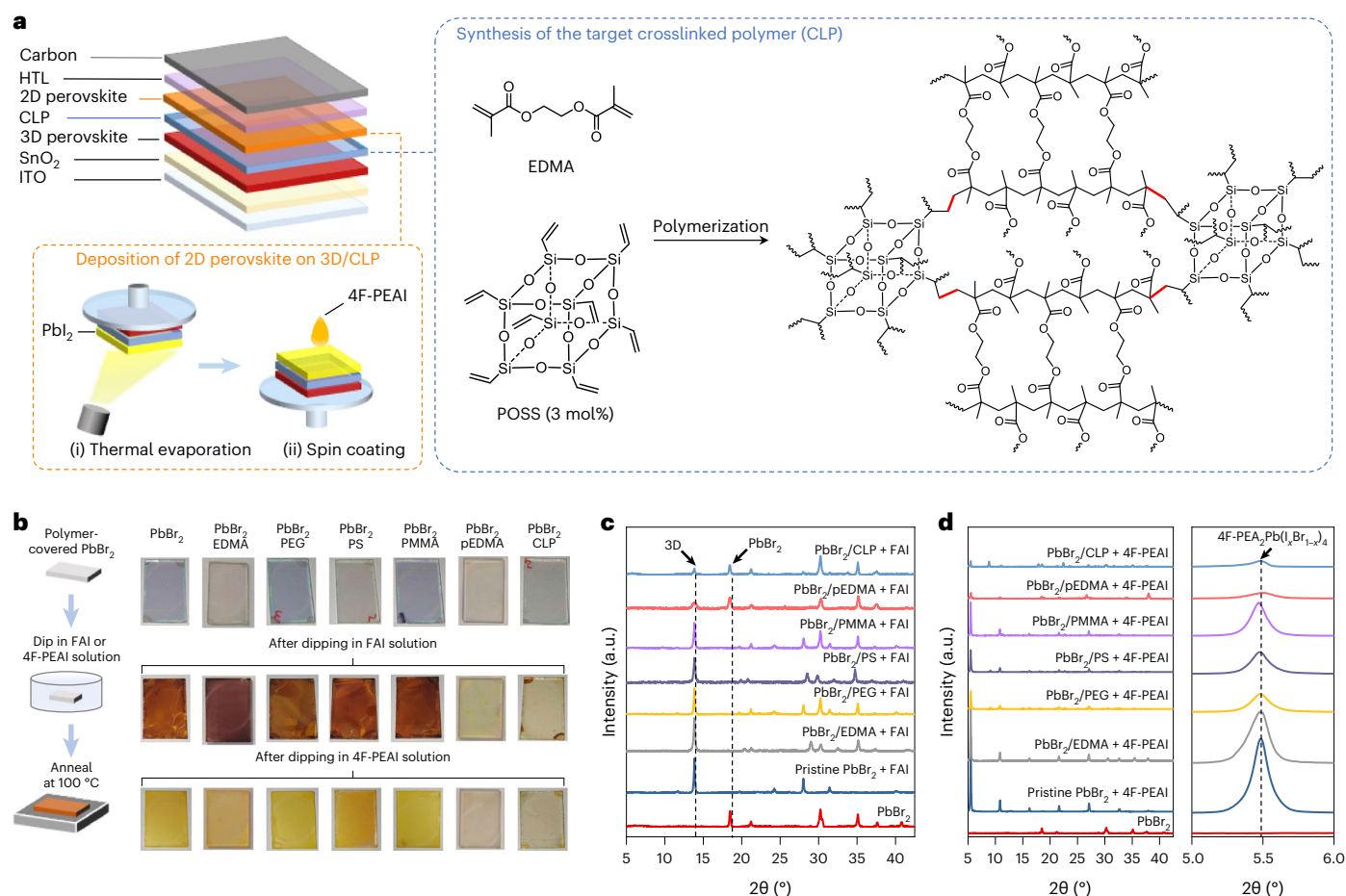


**Fig. 1** Preparation of the 3D/CLP/2D perovskite heterostructure and selection of CLP. **a**, Schematic of the device structure, the deposition of the 2D perovskite layer and the molecular structures and synthesis process of POSS, EDMA and the CLP. **b**, Schematic for investigating the effectiveness of different polymers at inhibiting ion diffusion. The polymer layer is deposited by spin coating PEG, PS, PMMA and CLP solutions (10 mg ml<sup>-1</sup>) at 1,000 r.p.m. for 20 s. Then the films are dipped either in a FAI solution (20 mg ml<sup>-1</sup> in IPA) or

4F-PEAI solution (20 mg ml<sup>-1</sup> in IPA). The photos of pristine PbBr<sub>2</sub> and PbBr<sub>2</sub> with different covering layers before and after dipping in FAI and 4F-PEAI solutions are shown for comparison. **c**, XRD patterns of pristine PbBr<sub>2</sub> and PbBr<sub>2</sub> covered with different polymers after dipping in the FAI solution. **d**, XRD patterns of pristine PbBr<sub>2</sub> and PbBr<sub>2</sub> covered with different polymers after dipping in the 4F-PEAI solution.

then a 4-fluorophenylethylammonium iodide (4F-PEAI)<sup>17,50</sup> solution (15 mmol in IPA) was spun on the above 3D/CLP/PbI<sub>2</sub> stacked film and annealed at 100 °C for 10 min (Supplementary Note 4 details the selection of 4F-PEAI).

XRD spectra in Fig. 2b show a stronger characteristic diffraction peak at 5.2° for the 3D/CLP/2D perovskite heterostructure than the 3D/2D perovskite heterostructure, which indicates the formation of a thicker 2D perovskite layer<sup>49,50</sup>. The cross-sectional SEM images show a ~500 nm 3D perovskite layer and a ~10 nm low-dimensional perovskite layer for the 3D/2D heterostructure and a ~500 nm 3D perovskite layer, a several nanometre CLP layer and a thicker ~30 nm 2D perovskite layer for the 3D/CLP/2D heterostructure (Fig. 2a). The XRD spectrum of the aged 3D/CLP/2D perovskite heterostructure shows that the characteristic diffraction peak at 5.2° remains relatively unchanged. A similar effect is observed for the PL spectra, where the PL emission peaks for the aged 3D/CLP/2D perovskite heterostructure retain their initial positions and intensities (Fig. 2c). A thick 2D perovskite layer was directly prepared on a 3D perovskite without the CLP layer by the same vapour-assisted two-step process as in the 3D/CLP/2D perovskite heterostructure. Notably, the red-shift PL peak position of the 2D perovskite in the 3D/thick 2D (vapour-deposited) heterostructure compared with the normal solution-processed 3D/2D heterostructure is attributed to the difference in thickness and quantum confinement effect<sup>50,54</sup>. The

intensity of the PL emission peak of 4F-PEAI<sub>2</sub>PbI<sub>4</sub> largely decreases, and a new peak corresponding to 4F-PEAI<sub>2</sub>FAPbI<sub>7</sub> (*n* = 2) appears after thermal ageing of the 3D/thick 2D heterostructure<sup>21,22</sup>. This indicates that the 3D/thick 2D heterostructure shows better stability than normal solution-processed 3D/2D heterostructure; however, its stability remains inferior to that of the 3D/CLP/2D perovskite heterostructure. The PL spectra of the heterostructure using EDMA as the interlayer showed similar behaviour with that of the 3D/thick 2D heterostructure (Fig. 2d). pEDMA as the interlayer resulted in suppression of the formation of the peak for 4F-PEAI<sub>2</sub>FAPbI<sub>4</sub>; however, the intensity of the PL emission peak of 4F-PEAI<sub>2</sub>PbI<sub>4</sub> still decreased. These results indicate that the CLP layer plays the dominant role of stabilizing the 3D/2D perovskite heterostructure under thermal stress.

To correlate the degradation of the 2D perovskite to ion diffusion, we employed atomic force microscopy-based infrared spectroscopy (AFM-IR) measurements to investigate the surface properties of the perovskite heterostructures. Imaging results were recorded at 1,712 cm<sup>-1</sup>, which corresponds to the symmetric C = NH<sub>2</sub><sup>+</sup> bending of FA<sup>+</sup>. As shown in Fig. 2e, initially, the 3D/2D perovskite heterostructure showed distinct signals of FA<sup>+</sup> cations, while there were low signals of FA<sup>+</sup> cations in the initial 3D/CLP/2D perovskite heterostructure. This indicated that the 2D perovskite layer in the 3D/CLP/2D perovskite heterostructure achieved more complete and uniform coverage on the



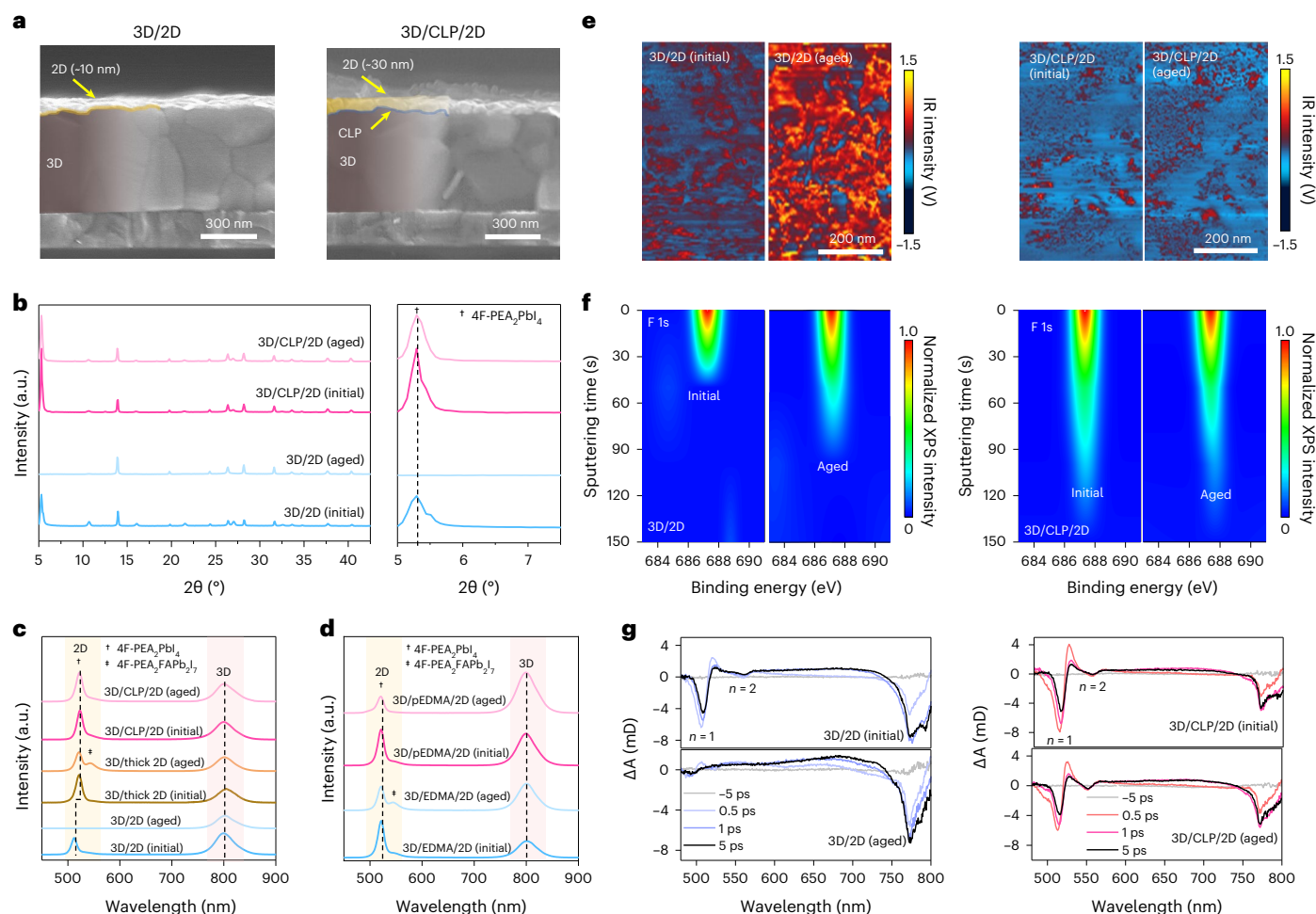


**Fig. 2 | Stabilization effect of the CLP on perovskite heterostructures.**

**a**, Cross-sectional SEM images of 3D/2D and 3D/CLP/2D perovskite heterostructures. The 3D, CLP and 2D perovskite are marked with gradient red colour, blue colour and gradient yellow colour. **b**, XRD patterns of initial and aged 3D/2D and 3D/CLP/2D perovskite heterostructures. **c**, Steady-state PL spectra of initial and aged (100 °C for 120 min) 3D/2D, 3D/thick 2D and 3D/CLP/2D perovskite heterostructures. The shaded orange and pink areas highlight the characteristic peaks of 2D and 3D perovskites for comparison. The thick 2D perovskite layer is prepared by the same vapour-assisted two-step process

as in the 3D/CLP/2D perovskite heterostructure. **d**, Steady-state PL spectra of initial and thermally aged 3D/EDMA/2D and 3D/pEDMA/2D perovskite heterostructures. **e**, AFM-IR (recorded at 1,712  $\text{cm}^{-1}$  corresponding to the symmetric C = NH<sub>2</sub><sup>+</sup> bending of FA<sup>+</sup>) images of 3D/2D and 3D/CLP/2D perovskite heterostructures before and after ageing at 100 °C for 120 min. **f**, XPS depth profiling of 3D/2D and 3D/CLP/2D perovskite heterostructures before and after ageing. **g**, TA spectra of 3D/2D and 3D/CLP/2D perovskite heterostructures before and after ageing.

3D perovskite layer than that in the 3D/2D perovskite heterostructure. After the perovskite heterostructures are aged at 100 °C for 120 min, the FA<sup>+</sup> signals largely increase on the surface of the 3D/2D perovskite heterostructure, which indicates the upward diffusion of FA<sup>+</sup> ions and the phase transformation from the 2D perovskite of 4F-PEA<sub>2</sub>PbI<sub>4</sub> into 3D perovskite during thermal stress. On the contrary, the 3D/CLP/2D perovskite heterostructure shows an almost unchanged FA<sup>+</sup> signal, which verifies the limited ion diffusion between the 3D and 2D perovskites and the enhanced stability of the 3D/CLP/2D heterostructure.

X-ray photoelectron spectroscopy (XPS) spectra show that the characteristic peaks of N in FA<sup>+</sup> for the 3D perovskite layer and 4F-PEA<sup>+</sup> for the 2D perovskite layer are at 400.8 eV and at 402.0 eV, respectively (Supplementary Fig. 9). XPS depth profiling in Fig. 2f shows that the characteristic peak of F in 4F-PEA<sup>+</sup> can be detected only on the top surface for -45 s. For the 3D/CLP/2D perovskite heterostructure, 4F-PEA<sup>+</sup> can be detected on the film surface for -120 s, which is also indicative of the thicker 2D layer in the 3D/CLP/2D perovskite heterostructure. Meanwhile, the downward diffusion of 4F-PEA<sup>+</sup> ions in the 3D/2D perovskite heterostructure is observed after thermal ageing, which is inhibited by the CLP layer in the 3D/CLP/2D heterostructure.

Furthermore, we conducted ultrafast transient absorption (TA) spectroscopy measurements of 3D/2D and 3D/CLP/2D perovskite heterostructures as shown in Fig. 2g<sup>55,56</sup>. Both initial perovskite heterostructures show the characteristic peaks at 773 nm from 3D perovskite, and at 515 nm from 2D perovskite 4F-PEA<sub>2</sub>PbI<sub>4</sub> ( $n = 1$ )<sup>56</sup>. Additionally, small  $n = 2$  2D perovskite peaks are also observed for the two heterostructures. This indicates that a small amount of FA<sup>+</sup> diffuses into the 2D perovskite through the CLP layer to form  $n = 2$  perovskites. After ageing at 100 °C for 120 min, the characteristic peak from 4F-PEA<sub>2</sub>PbI<sub>4</sub> ( $n = 1$ ) for the 3D/2D heterostructure almost completely vanished, while the peak for the 3D/CLP/2D heterostructure remained unchanged. Thus, we conclude that the CLP layer not only largely inhibits the ion (including both FA<sup>+</sup> and 4F-PEA<sup>+</sup>) diffusion between the stacked perovskite layers but also effectively stabilize the phase states of the 3D and 2D perovskites under thermal stress.

### Charge carrier dynamics and device performance

To investigate the carrier dynamics within the 3D/CLP/2D perovskite heterostructure and with perovskite/HTL stacks, we conducted time-resolved photoluminescence (TRPL) measurements. On glass

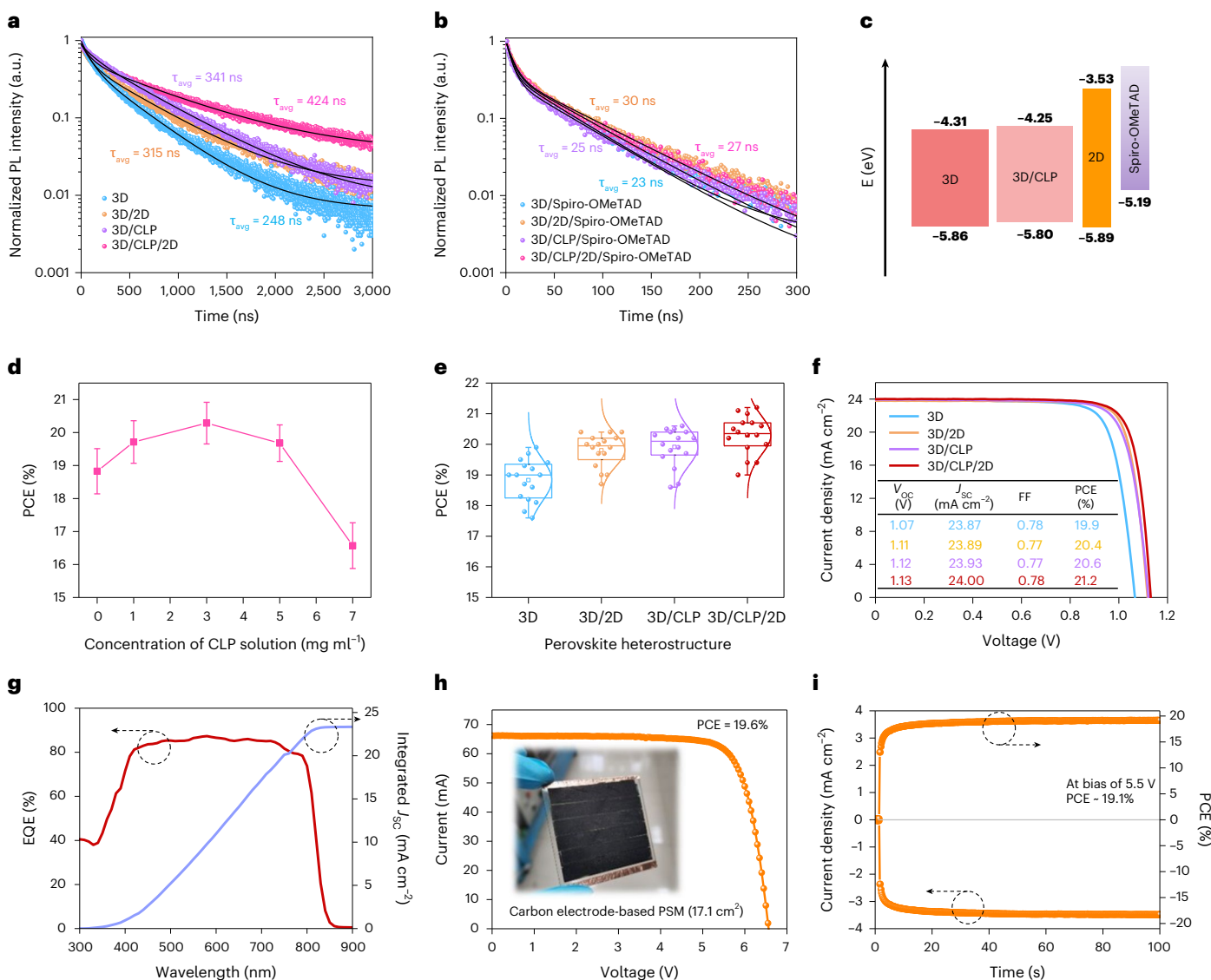


**Fig. 3 | Charge carrier dynamics and device performance. a**, TRPL spectra of 3D perovskite, 3D/2D, 3D/CLP and 3D/CLP/2D perovskite heterostructures on glass substrates. **b**, TRPL spectra of 3D perovskite, 3D/2D, 3D/CLP and 3D/CLP/2D perovskite heterostructures on spiro-OMeTAD. The measured spectra are fitted by bi-exponential decay function. **c**, Energy diagram of 3D perovskite, 3D/CLP, 2D perovskite and spiro-OMeTAD. **d**, Dependence of cell efficiency on the concentration of the CLP solution. Each average (symbol) and standard deviation (error bar) was calculated from 16 cells prepared at the same conditions. **e**, Distribution of efficiencies obtained by cells using 3D, 3D/2D, 3D/CLP and 3D/CLP/2D perovskite heterostructures. The standard error is represented in box

plots, for which the box extends from the 25th to the 75th percentiles; the empty squared dot depicts the average value; and the short dashed lines depict the minima and maxima. For each structure, 16 cells were fabricated at the same condition. **f**, Representative  $J$ - $V$  curves of PSCs fabricated using 3D perovskite, 3D/2D, 3D/CLP and 3D/CLP/2D perovskite heterostructures as the light-absorbing layer. **g**, External quantum efficiency spectrum and corresponding integrated current density of the champion cell based on the 3D/CLP/2D perovskite heterostructure. **h**,  $J$ - $V$  curves of the champion PSM based on the 3D/CLP/2D perovskite heterostructure. The inset shows a photograph of the PSM. **i**, The steady-state output and calculated PCE of the PSM at a fixed bias.

substrates, the 3D/2D perovskite heterostructure and the 3D/CLP film show longer average carrier lifetimes ( $\tau_{avg}$ ) (315 ns and 341 ns) than the pristine 3D perovskite (248 ns) (Fig. 3a and Supplementary Table 4). The  $\tau_{avg}$  of the 3D/CLP/2D perovskite heterostructure further increases to 423 ns. This is indicative of synergistic passivation from the CLP and 2D perovskite. When a 2,2',7,7'-tetrakis (*N,N*-di-*p*-methoxyphenyl-amine)-9,9'-spirobifluorene (spiro-OMeTAD) layer was deposited on top of the samples, the 3D perovskite, 3D/2D, 3D/CLP and 3D/CLP/2D perovskite heterostructures show similar  $\tau_{avg}$  and  $\tau_1$  (Fig. 3b). This indicates efficient charge extraction from the perovskites to the HTL can still be achieved after incorporating the CLP layer in the perovskite heterostructure. Consistent results were also obtained for the steady-state PL spectra (Supplementary Fig. 10). Space charge-limited current

spectra<sup>57–59</sup> of the perovskite heterostructures show that the 3D/2D and 3D/CLP/2D perovskite heterostructures generate current density–voltage ( $J$ - $V$ ) curves with similar shapes and comparable current values (Supplementary Figs. 11 and 12) for both electron-only and hole-only devices. By fitting the linear regions, the electron and hole mobilities of the 3D/CLP/2D heterostructure are similar compared with that of the 3D perovskite or 3D/2D heterostructure. Thus, the CLP layer has not hindered the transport of either the electrons or the holes within the heterostructures.

We conducted ultraviolet photoelectron spectroscopy (UPS) and ultraviolet–visible absorption spectroscopy (UV–vis) measurements to estimate the energy levels of the perovskite heterostructures (Supplementary Fig. 13). Compared with the 3D perovskite (FAPbI<sub>3</sub>)<sub>0.95</sub>(MA

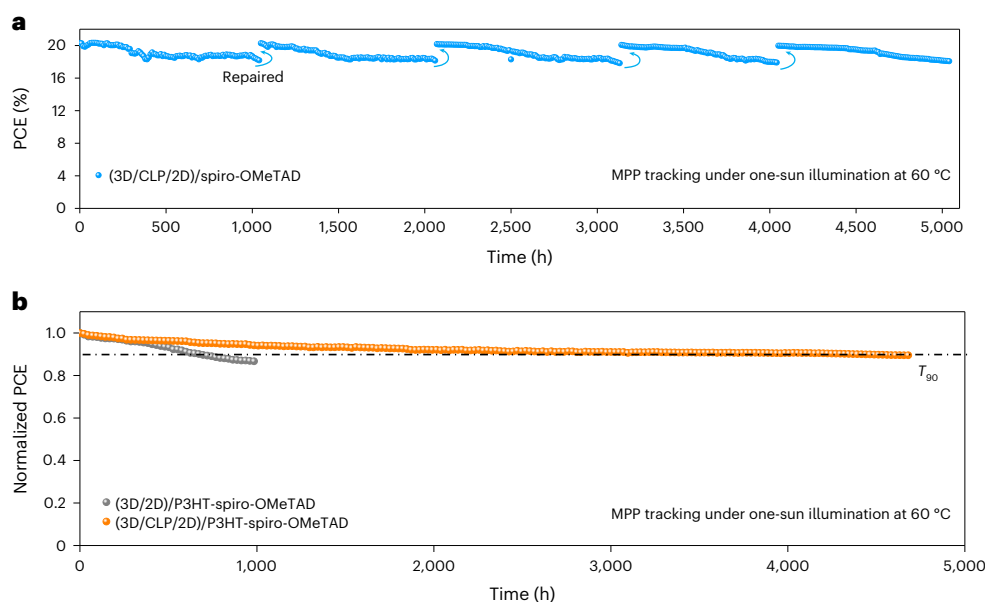


**Fig. 4 | Long-term stability test.** **a**, The operational stability of PSCs using spiro-OMeTAD as the HTL under continuous illumination in  $N_2$  at 60 °C. The cells are repaired by re-depositing the spiro-OMeTAD after every 1,000 hours of continuous illumination. **b**, The operational stability of PSCs using a mixed P3HT-

spiro-OMeTAD HTL under continuous illumination in  $N_2$  at 60 °C. The initial PCEs of the cells based on 3D/2D and 3D/CLP/2D perovskite heterostructures are 18.1% and 18.6%, respectively. The bias at the MPP was calculated and applied automatically.

$PbBr_3)_{0.05}$ , the incorporation of the CLP on the 3D perovskite leads to negligible change of the bandgap (1.55 eV), conduction band minimum and valence band maximum (Fig. 3c). The 2D perovskite 4F- $PEA_2PbI_4$  possesses a much larger bandgap of 2.36 eV and forms type-I band alignment with the 3D perovskite<sup>60</sup>. The close valence band maximum position of the 3D and 2D perovskites do not hinder the transport of holes from the 3D perovskite layer to the HTL<sup>10,11</sup>, while the higher conduction band minimum of the 2D perovskite than the 3D perovskite acts as an electron-blocking layer, effectively preventing the recombination of electrons in the perovskite and holes in the HTL for the 3D/2D and 3D/CLP/2D heterostructures<sup>10,13</sup>. This favourable band alignment contributes to the enhanced  $V_{OC}$  of as-fabricated cells, and the selection of 4F-PEAI is discussed in Supplementary Note 4.

To avoid the instability issues associated with metal electrodes<sup>36,61,62</sup>, we prepared carbon electrodes based on the screen-printing technique (Supplementary Fig. 14) to fabricate PSCs with a device architecture of ITO/SnO<sub>2</sub>/3D/CLP/2D/spiro-OMeTAD/carbon. We optimized the concentration of the CLP solution and found that the CLP layer prepared with a concentration of 3 mg ml<sup>-1</sup> delivered the optimal cell efficiency (Fig. 3d). We fabricated cells using 3D perovskite, 3D/2D, 3D/CLP and 3D/CLP/2D heterostructures as the light-absorbing layers, and the distribution of efficiencies is presented in Fig. 3e, Supplementary Table 5 and Supplementary Fig. 15. The cells based on 3D perovskite achieve an average efficiency of 18.83%. The average efficiencies of devices based on 3D/2D and 3D/CLP heterostructures are improved to 19.81% and 19.91%, respectively. The cells based on the 3D/CLP/2D heterostructure deliver an average efficiency of 20.29%. The efficiency improvement mainly results from the enhanced  $V_{OC}$ , which is attributed to the synergistic passivation effect of the CLP and 2D perovskite. Figure 3f shows the representative  $J-V$  curves of the cells. For the champion 3D/CLP/2D cell, we achieve a high efficiency of 21.2% with a  $V_{OC}$  of 1.13 V, a current density ( $J_{SC}$ ) of 24.00 mA cm<sup>-2</sup> and a FF of 0.78 for carbon-electrode-based PSCs (Supplementary Table 6). The steady-state power output (SPO) efficiency of the cell reaches ~20.87% (Supplementary Fig. 16). The external quantum efficiency spectrum of the 3D/CLP/2D PSC shows an integrated short-circuit current density

of 23.34 mA cm<sup>-2</sup> (Fig. 3g), which is in agreement with the  $J-V$  scanning result. We further fabricated a PSM with six sub-cells in series, as shown in Fig. 3h and Supplementary Fig. 17. The champion PSM based on the 3D/CLP/2D perovskite heterostructure with a carbon electrode and an aperture area of 17.1 cm<sup>2</sup> achieves a PCE of 19.6% with  $V_{OC}$  of 6.73 V, short-circuit current of 66.2 mA and FF of 0.751. Furthermore, it exhibits SPO efficiency of 19.1% under a bias voltage of 5.5 V for 100 s (Fig. 3i). Meanwhile, the PSM achieves a certified efficiency of 19.3% and SPO of 18.2% (Supplementary Fig. 18).

## Device stability

To study operational stability, we monitored the cell performance under MPP tracking conditions and continuous one-sun illumination at 60 °C (Supplementary Fig. 19). The estimated  $T_{90}$  lifetime of the 3D/2D PSC is 560 h. The PSC based on the 3D/CLP/2D perovskite heterostructure maintains ~92% of the initial efficiency after 1,000 hours under continuous illumination. According to time-of-flight secondary-ion mass spectrometry (TOF-SIMS) of these 1,000 h-aged cells, the diffusion of iodide ions from the perovskite layer to the spiro-OMeTAD layer is effectively suppressed in the 3D/CLP/2D PSC (Supplementary Fig. 20). Combined with the XPS depth profiling (Supplementary Fig. 21), we find that the CLP layer and 2D perovskite synergistically contribute to the suppressed diffusion of iodide.

To eliminate the negative effect of spiro-OMeTAD on the cell stability and verify the stability of the perovskite heterostructures, we carry out four repairing cycles of the cell by re-depositing the spiro-OMeTAD layer. The cell maintains ~90% of the initial efficiency after 5,000 h continuous operation (Fig. 4a). The cell performance recovery indicates that the 3D/CLP/2D perovskite heterostructure is highly stable against light and heat stress. Furthermore, a more stable poly(3-hexylthiophene)-spiro-OMeTAD (P3HT-spiro-OMeTAD) (3:1 w/w) mixed HTL is adopted to replace the unstable spiro-OMeTAD<sup>12</sup>. The initial efficiencies of as-fabricated PSCs slightly reduce to 18.6% based on 3D/CLP/2D perovskite heterostructure and 18.0% based on 3D/2D perovskite heterostructure (Supplementary Fig. 22). For the long-term operational stability, the efficiency of the 3D/2D PSC decays



to ~90% of the initial value after 672 h of continuous operation, while the 3D/CLP/2D PSC maintains 90% of its initial efficiency after continuous operation for 4,390 h at 60 °C (Fig. 4b).

## Conclusion

In summary, we successfully suppress the ion diffusion between surface 2D and bulk 3D perovskites by introducing a highly cross-linked network polymer. A highly stable 3D/CLP/2D perovskite heterostructure is constructed and combined with a carbon electrode to fabricate PSCs with an efficiency of 21.2% and mini-PSMs with an efficiency of 19.6% (certified stabilized efficiency of 18.2%). After 4,390 hours of continuous operation under MPP tracking and one-sun illumination, the device retains 90% of its initial performance.

## Methods

### Materials

All perovskite reagents including lead iodide (PbI<sub>2</sub>, 99.99%), formamidinium iodide (FAI, >99.5%), methylammonium bromide (MABr, >99.5%), lead bromide (PbBr<sub>2</sub>, 99.99%), methylammonium chloride (MACl, >99.5%), 4-fluorophenylethylammonium iodide (4F-PEAL, >99.5%), spiro-OMeTAD (99.5%) and poly(3-hexylthiophene) (P3HT) were purchased from Xi'an p-OLED Corp. Dimethylformamide (DMF, 99.8%), dimethyl sulfoxide (DMSO, 99.7%) and chlorobenzene (99.8%) were purchased from Acros. From Sigma-Aldrich, 4-tert-butylpyridine (96%), lithium bistrifluorosulfonyl imide (99.95%) and isopropanol (IPA, 99.99%) were obtained. The dimercaptosuccinic acid (DMSA, 98%), ethylene dimethacrylate (EDMA, 98%), octavinylotasilasesquioxane (POSS, 95%) and 2,2'-Azobis(2-methylpropionitrile) (AIBN, 98%) were purchased from Aladdin. The SnO<sub>2</sub> colloid dispersion was purchased from Alfa Aesar (tin (IV) oxide, 15 wt% in H<sub>2</sub>O colloidal dispersion). Graphite and carbon black powder were purchased from Aladdin. Indium tin oxide (ITO) (transmission >95%) substrates were purchased from South China Science & Technology Company Limited. Other materials were purchased from Aladdin and all the materials were used as received unless otherwise specified.

### Synthesis of the additive in carbon paste

1.0 g of DMSA (5.5 mmol), 0.99 g of ethylene dimethacrylate (EDMA) (5 mmol), 79.1 mg of octavinylotasilasesquioxane (POSS) (0.125 mmol) and 38 mg of 2,2-dimethoxy-2-phenylacetophenone (2 wt% of reactants) were well dispersed in the tetrahydrofuran (THF) (20 ml) in a quartz flask. The mixture was irradiated using a 365 nm UV lamp (25 W) for 2 h at room temperature. After the reaction was complete, *n*-hexane was added to obtain a solid crude product. The obtained product was dissolved in THF and precipitated in excess hexane again. Then, the solid was washed with deionized water and further dried under vacuum. Finally, 1.57 g of white additive powder was obtained.

### Preparation of the carbon electrode

Six g graphite, 2 g carbon black powder, 1.76 g of above additive powder and 0.8 g polyacrylate were mixed in the 2-butoxyethanol/pentyl acetate/ethyl acetate (volume ratio of 5:3:2) mixed solvents and kept ball milling for 12 h to obtain the carbon paste. The pre-prepared carbon paste was coated onto a carbon cloth via a screen-printing process to obtain the carbon film. The carbon paste/carbon cloth-based electrode was peeled off and then soaked in ethanol while sonicating for 10 min to remove the residual solvent. Finally, the carbon electrode was taken out and dried at room temperature.

### Fabrication of perovskite solar cells and mini-modules

ITO glass was patterned by laser etching (Universal Laser Systems, VLS2.30) with a femtosecond laser. Then the glass substrates were cleaned by sequential ultrasonication in a detergent solution, deionized water and anhydrous ethanol. The SnO<sub>2</sub> dispersion was spin coated on the substrates at 4,000 r.p.m. for 30 s and then annealed at 150 °C

for 30 min. After that, a 1.4 M (FAPbI<sub>3</sub>)<sub>0.95</sub>(MAPbBr<sub>3</sub>)<sub>0.05</sub> perovskite precursor solution containing of 0.5 M MACl was prepared in DMF/DMSO/GBL (v/v = 2:1:2). The perovskite precursor solution was spin coated on SnO<sub>2</sub> at 1,000 r.p.m. for 10 s and 5,000 r.p.m. for 20 s. The wet film was then immediately put into a sealed sample chamber connected to a home-built vacuum-pumping system and immediately exposed to low pressure (20 Pa) for 10 s. Subsequently, the perovskite film was put on a hotplate and annealed at 120 °C for 40 min to obtain the pristine 3D perovskite film. Next, 15 mM 4F-PEAL/IPA solution was spun on the above 3D perovskite at 4,000 r.p.m. for 30 s to prepare 3D/2D perovskite heterostructure. For the 3D/CLP/2D perovskite film, 3 mg EDMA, POSS (3 mol% of EDMA) and 2,2'-Azobis(2-methylpropionitrile) initiator (2 wt% of EDMA) were first dissolved in 1 ml of chlorobenzene and ethyl acetate mixed solution (v:v = 1:1) to prepare the CLP solution, and then spun on the above 3D perovskite at 4,000 r.p.m. for 30 s and annealed at 100 °C for 10 min. Then a 30 nm-thick layer of PbI<sub>2</sub> was evaporated at a rate of 0.3 Å s<sup>-1</sup> onto the 3D/CLP bilayer film in a vacuum chamber. Subsequently, the same concentration of 4F-PEAL/IPA solution was spun on the above 3D/CLP/PbI<sub>2</sub> film at 4,000 r.p.m. for 30 s and annealed at 100 °C for 10 min to prepare the 3D/CLP/2D perovskite heterostructure. After cooling down to room temperature, a HTL (73 mg ml<sup>-1</sup> spiro-OMeTAD in chlorobenzene with 9.36 mg Li-TFSI salt in acetonitrile and 30 μl 4-tert-butylpyridine) was deposited on the perovskite film by spin coating at 3,000 r.p.m. for 30 s. For the stability test, the P3HT-spiro-OMeTAD mixed HTL (54.75 mg P3HT and 18.25 mg spiro-OMeTAD with 4.68 mg Li-TFSI in acetonitrile and 15 μl 4-tert-butylpyridine) was deposited with the same spin-coating process. Finally, the pre-prepared carbon electrode was pressed onto the HTL under a pressure of 0.3 MPa at 60 °C for 15 s via a pneumatic hot press to complete the whole devices fabrication. For fabricating carbon-based modules, laser scribing was performed twice, before and after perovskite film deposition, to form P1 and P2 with 1,064 nm wavelength to complete the series interconnection between sub-cells in the module. Meanwhile, mechanical scribing was performed on the carbon electrode to obtain sub-electrode units insulated from each other before assembly. Finally, the electrode was pressed onto the HTL with the same process of small-area devices.

### Repairing of PSCs by re-depositing the HTL

The degraded PSCs were first disassembled to obtain the free-standing carbon electrode and perovskite/spiro-OMeTAD semi-cell. The spiro-OMeTAD on the semi-cell was washed out with chlorobenzene, followed by the deposition of the new spiro-OMeTAD HTL. Finally, the above disassembled carbon electrode was reassembled on the semi-cell to complete the repair of degraded PSCs.

### Characterization

The cross-sectional morphology of perovskite film was investigated by a field-emission scanning electron microscopy (FE-SEM, Hitachi SU8010). The TRPL spectra were measured by a HORIBA Jobin-Yvon Fluorolog-III fluorimeter. The steady-state PL spectra were measured with a 405 nm wavelength excitation source and the PL emission was collected using an optical fibre coupled with an Ocean Optics spectrometer ('Flame') calibrated by the manufacturer. UV-vis absorption of perovskite films was measured by UV-vis spectrometer (lambda 750 S, PerkinElmer). Thermogravimetric analysis was carried out using a TA Instruments TGA 2050 thermogravimetric analyser. The XRD patterns were collected from X-ray diffractometer (D8 Advance). AFM-IR experiments were carried out using a commercial AFM-IR set-up (NanoIR3s, Bruker) that consists of an AFM microscope operating in contact mode and a Quantum Cascade Laser or QCL laser (MIRcat, Daylight Solutions Inc.) that was tunable from 2,350 cm<sup>-1</sup> to ~870 cm<sup>-1</sup> (from 4.25 μm to 11.49 μm). The *J*-*V* curves were measured using a solar simulator (Oriel 94023 A, 300 W) with a source meter (Keithley 2400) under 100 mW cm<sup>-2</sup> illumination (AM 1.5 G) with a scan rate of

100 mV s<sup>-1</sup> for solar cells and 500 mV s<sup>-1</sup> for modules. The small-area PSCs and large-area PSMs are measured using masks with an area of 0.16 cm<sup>2</sup> and 17.1 cm<sup>2</sup>, respectively.

### FTIR measurement

The polymer monomers were first polymerized on the perovskite surface, and then the sample was cleaned with DMF solution and dried under vacuum to remove the perovskite material. The IR spectra were recorded with a VERTEX 70 Infrared Fourier transform microscope (Bruker Co.).

### XPS measurement

XPS measurements were performed with a PHI VersaProbe II scanning XPS microprobe using a monochromatic Al K $\alpha$  X-ray of 24.8 W power with a beam size of 100  $\mu$ m. All peaks were calibrated using C 1s peak at 284.8 eV to correct charge shift of binding energies.

### PES measurement

The PES measurements were performed on the ThermoFisher ESCALAB Xi<sup>+</sup> system. For reference, the XPS/UPS spectra energy positions were calibrated using a standard Au sample at BE of Au 4f<sub>7/2</sub> = 84.0 eV and EF = 0 eV. The gas cluster ion beam sputtering parameters were set as 2,000 sizes at 4 keV mode with a 5 mm sputtering spot. XPS measurements were carried out using monochromated Al K $\alpha$  source ( $h\nu = 1,486.6$  eV, where  $h$  is the Planck's constant and  $\nu$  is the photon frequency) with a pass energy of 20 eV. UPS measurements were performed using a He UV lamp ( $h\nu = 21.2$  eV) with a pass energy of 1 eV.

### TOF-SIMS measurements

Compositional depth profiling of perovskite films was carried out using a TOF-SIMS 5 system from IONTOF, operated in the spectral mode and using a 30 keV Bi<sup>3+</sup> primary ion beam with an ion current of 0.8 pA. For depth profiling, a 1 keV Cs<sup>+</sup> sputter beam with a current of 28 nA was used to remove material layer by layer in interlaced mode, from a raster area of 300  $\mu$ m  $\times$  300  $\mu$ m. Mass spectrometry was performed on an area of 80  $\mu$ m  $\times$  80  $\mu$ m in the centre of the sputter crater.

### TA measurements

Femtosecond laser pulses of 800 nm fundamental beam (5 kHz repetition rate, 35 fs pulse width) were produced using a Ti:Sapphire regenerative amplifier (Legend Duo, Coherent Inc.). Part of the fundamental beam was used to pump an optical parametric amplifier (TOPAS-Prime, Light Conversion) to serve as a narrow-band pump, while the other part was focused on a sapphire crystal to generate a white light supercontinuum probe (420–780 nm window with various optical filters). The pump wavelength was 400 nm under pump power of 3  $\mu$ J cm<sup>-2</sup>. Both the pump and probe pulses were directed into a commercial TA spectrometer (Helios, Ultrafast Systems). Delaying the probe pulse relative to the pump pulse provides a time window of up to 8 ns. The instrument response function was determined to be  $\sim$ 200 fs by a routine cross-correlation procedure. All TA spectra were chirp corrected.

### Stability test

For the stability tests of 3D/2D perovskite heterostructure, all samples were aged at 100 °C for 120 min under nitrogen atmosphere. The operational stability tests were carried out at the MPP for the encapsulated cells under one-sun illumination (100 mW cm<sup>-2</sup>). The cells were tested in a chamber with an ambient atmosphere temperature of  $\sim$ 60 °C. The bias at the MPP was calculated and applied automatically. The cells were encapsulated in a N<sub>2</sub>-filled glovebox. A hot melt film was attached around the active area of the cells, and a glass slide was employed as the back sheet. Then the sample (cell/hot melt film/glass slide) was heated at 100 °C under a vacuum condition ( $<100$  Pa) for 15 min by a commercial laminating system.

### Reporting summary

Further information on research design is available in the Nature Portfolio Reporting Summary linked to this article.

### Data availability

All the data supporting the findings of this study are available within this article and its Supplementary Information. Any additional information can be obtained from corresponding authors upon request. Source data are provided with this paper.

### References

1. Min, H. et al. Perovskite solar cells with atomically coherent interlayers on SnO<sub>2</sub> electrodes. *Nature* **598**, 444–450 (2021).
2. Jeong, J. et al. Pseudo-halide anion engineering for  $\alpha$ -FAPbI<sub>3</sub> perovskite solar cells. *Nature* **592**, 381–385 (2021).
3. Yoo, J. J. et al. Efficient perovskite solar cells via improved carrier management. *Nature* **590**, 587–593 (2021).
4. *Best Research-Cell Efficiency Chart* (National Renewable Energy Laboratory, 2021); <https://www.nrel.gov/pv/cell-efficiency.html>
5. Bu, T. et al. Lead halide-templated crystallization of methylamine-free perovskite for efficient photovoltaic modules. *Science* **372**, 1327–1332 (2021).
6. Chen, S. et al. Stabilizing perovskite–substrate interfaces for high-performance perovskite modules. *Science* **373**, 902–907 (2021).
7. Deng, Y. et al. Defect compensation in formamidinium-caesium perovskites for highly efficient solar mini-modules with improved photostability. *Nat. Energy* **6**, 633–641 (2021).
8. Liu, Y. et al. Ultrahydrophobic 3D/2D fluoroarene bilayer-based water-resistant perovskite solar cells with efficiencies exceeding 22%. *Sci. Adv.* **5**, eaaw2543 (2019).
9. Alharbi, E. A. et al. Atomic-level passivation mechanism of ammonium salts enabling highly efficient perovskite solar cells. *Nat. Commun.* **10**, 3008 (2019).
10. Jang, Y.-W. et al. Intact 2D/3D halide junction perovskite solar cells via solid-phase in-plane growth. *Nat. Energy* **6**, 63–71 (2021).
11. Tan, S. et al. Stability-limiting heterointerfaces of perovskite photovoltaics. *Nature* **605**, 268–273 (2022).
12. Liu, Z. et al. A holistic approach to interface stabilization for efficient perovskite solar modules with over 2,000-hour operational stability. *Nat. Energy* **5**, 596–604 (2020).
13. Sidhik, S. et al. Deterministic fabrication of 3D/2D perovskite bilayer stacks for durable and efficient solar cells. *Science* **377**, 1425–1430 (2022).
14. Yang, G. et al. Stable and low-photovoltage-loss perovskite solar cells by multifunctional passivation. *Nat. Photon.* **15**, 681–689 (2021).
15. Zhang, F. et al. Metastable Dion–Jacobson 2D structure enables efficient and stable perovskite solar cells. *Science* **375**, 71–76 (2021).
16. Azmi, R. et al. Damp heat-stable perovskite solar cells with tailored-dimensionality 2D/3D heterojunctions. *Science* **376**, 73–77 (2022).
17. Chen, H. et al. Quantum-size-tuned heterostructures enable efficient and stable inverted perovskite solar cells. *Nat. Photon.* **16**, 352–358 (2022).
18. Proppe, A. H. et al. Multication perovskite 2D/3D interfaces form via progressive dimensional reduction. *Nat. Commun.* **12**, 3472 (2021).
19. Huang, Z. et al. Suppressed ion migration in reduced-dimensional perovskites improves operating stability. *ACS Energy Lett.* **4**, 1521–1527 (2019).
20. Yoo, J. J. et al. An interface stabilized perovskite solar cell with high stabilized efficiency and low voltage loss. *Energy Environ. Sci.* **12**, 2192–2199 (2019).



21. Sutanto, A. A. et al. In situ analysis reveals the role of 2D perovskite in preventing thermal-induced degradation in 2D/3D perovskite interfaces. *Nano Lett.* **20**, 3992–3998 (2020).
22. Sutanto, A. A. et al. Dynamical evolution of the 2D/3D interface: a hidden driver behind perovskite solar cell instability. *J. Mater. Chem. A* **8**, 2343–2348 (2020).
23. Mosconi, E. et al. Mobile ions in organohalide perovskites: interplay of electronic structure and dynamics. *ACS Energy Lett.* **1**, 182–188 (2016).
24. Motti, S. G. et al. Defect activity in lead halide perovskites. *Adv. Mater.* **31**, 1901183 (2019).
25. Zhou, Y. et al. Defect activity in metal halide perovskites with wide and narrow bandgap. *Nat. Rev. Mater.* **6**, 986–1002 (2021).
26. Chen, J. et al. Stabilizing the Ag electrode and reducing  $J-V$  hysteresis through suppression of iodide migration in perovskite solar cells. *ACS Appl. Mater. Interfaces* **9**, 36338–36349 (2017).
27. Grancini, G. et al. Dimensional tailoring of hybrid perovskites for photovoltaics. *Nat. Rev. Mater.* **4**, 4–22 (2019).
28. Lee, J.-W. et al. 2D perovskite stabilized phase-pure formamidinium perovskite solar cells. *Nat. Commun.* **9**, 3021 (2018).
29. Luo, C. et al. Facet orientation tailoring via 2D-seed-induced growth enables highly efficient and stable perovskite solar cells. *Joule* **6**, 240–257 (2022).
30. Bi, E. et al. Mitigating ion migration in perovskite solar cells. *Trends Chem.* **3**, 575–588 (2021).
31. Bai, S. et al. Planar perovskite solar cells with long-term stability using ionic liquid additives. *Nature* **571**, 245–250 (2019).
32. Yuan, Y. et al. Ion migration in organometal trihalide perovskite and its impact on photovoltaic efficiency and stability. *Acc. Chem. Res.* **49**, 286–293 (2016).
33. Lee, J.-W. et al. Verification and mitigation of ion migration in perovskite solar cells. *APL Mater.* **7**, 041111 (2019).
34. Li, N. et al. Cation and anion immobilization through chemical bonding enhancement with fluorides for stable halide perovskite solar cells. *Nat. Energy* **4**, 408–415 (2019).
35. Bi, E. et al. Efficient perovskite solar cell modules with high stability enabled by iodide diffusion barriers. *Joule* **3**, 2748–2760 (2019).
36. Wang, Y. et al. Stabilizing heterostructures of soft perovskite semiconductors. *Science* **365**, 687–691 (2019).
37. Lin, X. et al. In situ growth of graphene on both sides of a Cu–Ni alloy electrode for perovskite solar cells with improved stability. *Nat. Energy* **7**, 520–527 (2022).
38. Li, Z. et al. Organometallic-functionalized interfaces for highly efficient inverted perovskite solar cells. *Science* **376**, 416–420 (2022).
39. Yang, S. et al. Stabilizing halide perovskite surfaces for solar cell operation with wide-bandgap lead oxysalts. *Science* **365**, 473–478 (2019).
40. Chen, H. et al. The research progress of polyhedral oligomeric silsesquioxane (POSS) applied to electrical energy storage elements. *Funct. Mater. Lett.* **10**, 1730001 (2017).
41. Pan, H. et al. Organic–inorganic hybrid proton exchange membrane based on polyhedral oligomeric silsesquioxanes and sulfonated polyimides containing benzimidazole. *J. Power Sources* **263**, 195–202 (2014).
42. Li, Z. et al. In situ implantation of cross-linked functional POSS blocks in Nafion® for high performance direct methanol fuel cells. *J. Membr. Sci.* **640**, 119798 (2021).
43. Ma, J. et al. Dipentaerythritol penta-/hexa-acrylate based-highly cross-linked hybrid monolithic column: Preparation and its applications for ultrahigh efficiency separation of proteins. *Anal. Chim. Acta* **963**, 143–152 (2017).
44. Xu, H. et al. Preparation,  $T_g$  improvement, and thermal stability enhancement mechanism of soluble poly(methyl methacrylate) nanocomposites by incorporating octavinyl polyhedral oligomeric silsesquioxanes. *J. Polym. Sci. Pol. Chem.* **45**, 5308–5317 (2007).
45. Cao, Q. et al. Star-polymer multidentate-cross-linking strategy for superior operational stability of inverted perovskite solar cells at high efficiency. *Energy Environ. Sci.* **4**, 5406–5415 (2021).
46. Cao, Q. et al. Efficient and stable inverted perovskite solar cells with very high fill factors via incorporation of star-shaped polymer. *Sci. Adv.* **7**, eabg0633 (2021).
47. Chen, L. et al. Intrinsic phase stability and inherent bandgap of formamidinium lead triiodide perovskite single crystals. *Angew. Chem. Int. Ed.* **61**, e202212700 (2022).
48. Lu, H. et al. Vapor-assisted deposition of highly efficient, stable black-phase FAPbI<sub>3</sub> perovskite solar cells. *Science* **370**, eabb8985 (2020).
49. Kikuchi, K. et al. Structure and optical properties of lead iodide based two-dimensional perovskite compounds containing fluorophenethylamines. *Curr. Appl. Phys.* **4**, 599–602 (2004).
50. Zhou, Q. et al. High-performance perovskite solar cells with enhanced environmental stability based on a (*p*-FC<sub>6</sub>H<sub>4</sub>C<sub>2</sub>H<sub>4</sub>NH<sub>3</sub>)<sub>2</sub>[PbI<sub>4</sub>] capping layer. *Adv. Energy Mater.* **9**, 1802595 (2019).
51. Luo, L. et al. Large-area perovskite solar cells with Cs<sub>x</sub>FA<sub>1-x</sub>PbI<sub>3-y</sub>Br<sub>y</sub> thin films deposited by a vapor-solid reaction method. *J. Mater. Chem. A* **6**, 21143–21148 (2018).
52. Luo, L. et al. 19.59% efficiency from Rb<sub>0.04</sub>-Cs<sub>0.14</sub>FA<sub>0.86</sub>Pb(Br<sub>y</sub>I<sub>1-y</sub>)<sub>3</sub> perovskite solar cells made by vapor-solid reaction technique. *Sci. Bull.* **66**, 962–964 (2021).
53. Li, H. et al. Sequential vacuum-evaporated perovskite solar cells with more than 24% efficiency. *Sci. Adv.* **8**, eabo7422 (2022).
54. Cho, K. T. et al. Selective growth of layered perovskites for stable and efficient photovoltaics. *Energy Environ. Sci.* **11**, 952–959 (2018).
55. Quintero-Bermudez, R. et al. Compositional and orientational control in metal halide perovskites of reduced dimensionality. *Nat. Mater.* **17**, 900–907 (2018).
56. Hu, J. et al. Synthetic control over orientational degeneracy of spacer cations enhances solar cell efficiency in two-dimensional perovskites. *Nat. Commun.* **10**, 1276 (2019).
57. Le Corre, V. M. et al. Revealing charge carrier mobility and defect densities in metal halide perovskites via space-charge-limited current measurements. *ACS Energy Lett.* **6**, 1087–1094 (2021).
58. Sajedi Alvar, M. et al. Space-charge-limited electron and hole currents in hybrid organic-inorganic perovskites. *Nat. Commun.* **11**, 4023 (2020).
59. Shi, D. et al. Low trap-state density and long carrier diffusion in organolead trihalide perovskite single crystals. *Science* **347**, 519–522 (2015).
60. Wang, T. et al. Recent progress on heterojunction engineering in perovskite solar cells. *Adv. Energy Mater.* <https://doi.org/10.1002/aenm.202201436> (2022).
61. Domanski, K. et al. Not all that glitters is gold: metal-migration-induced degradation in perovskite solar cells. *ACS Nano* **10**, 6306–6314 (2016).
62. Zhang, C. et al. Ti<sub>1</sub>-graphene single-atom material for improved energy level alignment in perovskite solar cells. *Nat. Energy* **6**, 1154–1163 (2021).

## Acknowledgements

This work was financially supported by National Key Research and Development Program of China (2020YFA0715000, L.M.; 2022YFB4200305, X.L. and Y.R.); National Natural Science Foundation of China (21875081, X.L.; 22279039, X.L.; 52172200, Y.R. and 52127816, L.M.); the Chinese National 1000-Talent-Plan programme (X.L.); the Science and Technology Department of Hubei Province (2021CFB315, Y.R.); the Innovation Project of Optics Valley Laboratory OVL2021BG008 (X.L.); the foundation of State Key Laboratory of

New Textile Materials and Advanced Processing Technologies (grant number FZ2021011, X.L.), the Foundation of State Key Laboratory of Coal Conversion (grant number J18-19-913, X.L.). We thank the Analytical and Testing Center from HUST and the Center for Nanoscale Characterization and Devices (CNCD) from WNLO (HUST) for the facility support of sample measurements. We would like to thank Suzhou Institute of Nano-Tech and Nano-Bionics for performing TOF-SIMS. Z.W. acknowledges the Banting Postdoctoral Fellowships Program of Canada.

### Author contributions

X.L. directed and supervised the project. L. Luo, Z.W. and Y.R. designed the experiments. L. Luo fabricated the perovskite devices. H.Z. synthesized polymer materials. L. Luo, M.L. and S.Y. contributed to the certification of mini-modules. Q.A. and L.C., conducted XRD and XPS measurements. W. Li and L. Luo carried out SEM and PL measurements. D.L. and J.H. conducted UPS and XPS measurements. L. Luo and H.Z. conducted FTIR measurements. L. Li conducted AFM-IR measurement. R.G. conducted the stability tests on the devices. R.H. conducted TOF-SIMS measurement. X.C. and W. Liang conducted TA measurements. L. Luo wrote the first draft of the manuscript. X.L, E.H.S., Y.R., L.M., Z.W., B.C., A.M. and H.Z. revised the manuscript. All authors analysed the data and reviewed the manuscript.

### Competing interests

The authors declare no competing interests.

### Additional information

**Supplementary information** The online version contains supplementary material available at <https://doi.org/10.1038/s41560-023-01205-y>.

**Correspondence and requests for materials** should be addressed to Liqiang Mai, Yaoguang Rong, Edward H. Sargent or Xiong Li.

**Peer review information** *Nature Energy* thanks Michael McGehee and the other, anonymous, reviewer(s) for their contribution to the peer review of this work.

**Reprints and permissions information** is available at [www.nature.com/reprints](http://www.nature.com/reprints).

**Publisher's note** Springer Nature remains neutral with regard to jurisdictional claims in published maps and institutional affiliations.

Springer Nature or its licensor (e.g. a society or other partner) holds exclusive rights to this article under a publishing agreement with the author(s) or other rightsholder(s); author self-archiving of the accepted manuscript version of this article is solely governed by the terms of such publishing agreement and applicable law.

© The Author(s), under exclusive licence to Springer Nature Limited 2023

## Solar Cells Reporting Summary

Nature Research wishes to improve the reproducibility of the work that we publish. This form is intended for publication with all accepted papers reporting the characterization of photovoltaic devices and provides structure for consistency and transparency in reporting. Some list items might not apply to an individual manuscript, but all fields must be completed for clarity.

For further information on Nature Research policies, including our [data availability policy](#), see [Authors & Referees](#).

### Experimental design

Please check: are the following details reported in the manuscript?

#### 1. Dimensions

Area of the tested solar cells  Yes  No The area of small tested solar cells is 0.16 cm<sup>2</sup>, and the area of large solar modules is 17.1 cm<sup>2</sup>. (Methods - Device characterization)

Method used to determine the device area  Yes  No Shading masks were used to determine the aperture area of the tested solar cells and solar modules.

#### 2. Current-voltage characterization

Current density-voltage (J-V) plots in both forward and backward direction  Yes  No Supplementary Figure 16.

Voltage scan conditions  Yes  No The JV curves were measured with a scan rate of 100 mV/s (voltage step of 10 mV and delay time of 100 ms) for the small solar cells. For the solar modules, the scan rate is 500 mV/s (voltage step of 100 mV and delay time of 100 ms) (Methods - Device characterization)  
*For instance: scan direction, speed, dwell times*

Test environment  Yes  No Unencapsulated cells were tested in a nitrogen environment. Encapsulated cells were tested in ambient air (Methods - Device characterization)  
*For instance: characterization temperature, in air or in glove box*

Protocol for preconditioning of the device before its characterization  Yes  No No preconditioning was used

Stability of the J-V characteristic  Yes  No Maximum power point tracking (Figure 3i, 4a, 4b and Supplementary Figure 16, 19)  
*Verified with time evolution of the maximum power point or with the photocurrent at maximum power point; see ref. 7 for details.*

#### 3. Hysteresis or any other unusual behaviour

Description of the unusual behaviour observed during the characterization  Yes  No Cells show negligible hysteresis (Supplementary Figure 16)

Related experimental data  Yes  No Supplementary Figure 16

#### 4. Efficiency

External quantum efficiency (EQE) or incident photons to current efficiency (IPCE)  Yes  No Figure 3g

A comparison between the integrated response under the standard reference spectrum and the response measure under the simulator  Yes  No Figure 3g

For tandem solar cells, the bias illumination and bias voltage used for each subcell  Yes  No This report does not include tandem solar cells

#### 5. Calibration

Light source and reference cell or sensor used for the characterization  Yes  No Newport solar simulator (Class A, Oriel 94023A) is used for the measurements



Confirmation that the reference cell was calibrated and certified	<input checked="" type="checkbox"/> Yes <input type="checkbox"/> No	The light intensity was calibrated by a reference solar cell by Newport (Methods - Device characterization)
Calculation of spectral mismatch between the reference cell and the devices under test	<input type="checkbox"/> Yes <input checked="" type="checkbox"/> No	No spectral mismatch calculation was performed.
<b>6. Mask/aperture</b>		
Size of the mask/aperture used during testing	<input checked="" type="checkbox"/> Yes <input type="checkbox"/> No	0.16 cm <sup>2</sup> for small-area solar cells, and 17.1 cm <sup>2</sup> for solar modules (Methods - Device characterization)
Variation of the measured short-circuit current density with the mask/aperture area	<input type="checkbox"/> Yes <input checked="" type="checkbox"/> No	We did not evaluate multiple testing apertures
<b>7. Performance certification</b>		
Identity of the independent certification laboratory that confirmed the photovoltaic performance	<input checked="" type="checkbox"/> Yes <input type="checkbox"/> No	Certification was carried out by the National Institute of Metrology in China (Supplementary Figure 18)
A copy of any certificate(s) <i>Provide in Supplementary Information</i>	<input checked="" type="checkbox"/> Yes <input type="checkbox"/> No	Supplementary Figure 18
<b>8. Statistics</b>		
Number of solar cells tested	<input checked="" type="checkbox"/> Yes <input type="checkbox"/> No	Statistical analysis was performed on 16 devices of each architecture (Figure 3e, Supplementary Figure 15)
Statistical analysis of the device performance	<input checked="" type="checkbox"/> Yes <input type="checkbox"/> No	Supplementary Figure 15
<b>9. Long-term stability analysis</b>		
Type of analysis, bias conditions and environmental conditions <i>For instance: illumination type, temperature, atmosphere humidity, encapsulation method, preconditioning temperature</i>	<input checked="" type="checkbox"/> Yes <input type="checkbox"/> No	Stability tests were performed under 1-sun illumination at maximum power point tracking condition. The test was performed in a light soaking chamber with an ambient atmosphere temperature of 60 degree Celsius. The bias at maximum power point was calculated and applied automatically. (Figure 4a and b, Methods - Stability test)